SAND2014-3590J

SAND Number: 2014-0683

Detection of preferential particle orientation in the atmosphere: development of an alternative polarization lidar system

Manfred Geier*, Marco Arienti*

Sandia National Laboratories, Livermore, CA 94551

Abstract

Increasing interest in polarimetric characterization of atmospheric aerosols has led to the development of complete sample-measuring (Mueller) polarimeters that are capable of measuring the entire backscattering phase matrix of a probed volume. These Mueller polarimeters consist of several moving parts, which limit measurement rates and complicate data analysis. In this article, we present the concept of a less complex polarization lidar setup for detection of preferential orientation of atmospheric particulates. On the basis of theoretical considerations of data inversion stability and propagation of measurement uncertainties, an optimum optical configuration is established for two modes of operation (with either a linear or a circular polarized incident laser beam). The conceptualized setup falls in the category of incomplete sample-measuring polarimeters and uses four detection channels for simultaneous measurement of the backscattered light. The expected performance characteristics are discussed through an example of a typical aerosol with a small fraction of particles oriented in a preferred direction. The theoretical analysis suggests that achievable accuracies in backscatter cross-sections and depolarization ratios are similar to those with conventional two-channel configurations, while in addition preferential orientation can be detected with the proposed four-channel system for a wide range of conditions.

Keywords: Light scattering, Remote sensing, Lidar, Polarization, Aerosol

1. Introduction

Lidar techniques have been applied since the late 1960's and have become indispensable tools for characterization of the atmosphere [1]. The laser light used to interrogate the atmosphere leaves the dynamics of the probed fluid unperturbed and therefore enables characterization of conditions in the atmosphere with high temporal and spatial resolution. Polarization lidar systems provide information on changes in the polarization state induced by the scatterers in the probed volume element, which are commonly quantified in terms of changes in the overall backscatter coefficient and in the linear (or circular) depolarization ratio [2]. The backscatter coefficient quantifies the amount of light scattered into the backward direction and thus characterizes the optical properties of a probed region in the atmosphere [1]. Depolarization ratios have been used extensively to discriminate between ice and water phases in clouds [2–8], and serve as indicators for multiple scattering and for the presence and discrimination of nonspherical scatterers [9, 10]. Preferential orientation of nonspherical particles may result in significantly higher (or lower) effective cross-sections for extinction of incident radiation than expected from orientation-averaged cross-sections, and may thus cause significantly more (or less) participation in radiative energy exchange. An example reported in this paper shows that the scattering cross-sections for the studied particles vary over more two orders of magnitude depending on the particle orientation relative to the propagation direction of the incident light.

Kaul *et al.* [11] showed with their measurements of the backscatter phase matrix that large hexagonal faces of ice crystals in cirrus clouds tend to align with a horizontal plane, and produce visually observable sundogs and light pillars. Airborne particulates, mostly inorganic dust particles, biogenic particles, and soot aggregates [12], are considerably smaller than ice crystals (a few nanometers to several micrometers versus tens of micrometers to several millimeters) [13], and typically have nonspherical shapes. For theses particulates, gravitational, fluid

*Corresponding author.

Email addresses: manfred.geier@gmx.net (Manfred Geier), marient@sandia.gov (Marco Arienti)

dynamic, electric and magnetic forces have conveniently been assumed to be ineffective in producing appreciable particle orientation, but the validity of that assumption has been questioned in recent years based on theoretical considerations and experimental evidence [14, 15]. Whether caused by preferential orientation or by insufficient population size (when the number of particles of a kind is too small for each sampled particle to have a particle in reciprocal orientation present), an imbalance in the particulate orientation may lead to erroneous interpretation of depolarization ratios. Measurements sensitive to detecting particle ordering therefore complement traditional depolarization measurements and could provide valuable insight into atmospheric aerosol dynamics, enabling better, unbiased interpretation of lidar returns.

Over the past forty years, the merits of measured depolarization ratios in the characterization of atmospheric aerosols have led to wide-spread application of polarization lidar systems in various configurations. Early systems fall into the category of Stokes polarimeters (or light-measuring polarimeters [16]), which measure the polarization states of the returning light. For instance, Pal and Carswell used a three-channel system to determine the first three Stokes parameters I, Q, U [17]. A four-channel Stokes polarimeter has been investigated by Houston and Carswell [18], who, based on their findings, concluded that the increased complexity outweighs the benefits of four-component measurements and recommended two-channel measurements as the most efficient lidar approach [18]. The system described in [3] uses two channels for detection, but it is capable of measuring the full Stokes vector of the backscattered light by utilizing three switchable ferroelectric cells together with a quarter-wave plate to vary the polarization states for signal generation and analysis. The instrument allows for quasi-simultaneous measurement of both linear and circular depolarization ratio, and was proposed mainly for detection of oriented ice platelets in clouds. A single-detector system with similarly switched polarization states of the incident beam is described in [19].

Mueller-matrix polarimetric lidar systems for measurement of the entire backscatter matrix have been described by Kaul *et al.* [11], and more recently by Hayman *et al.* [20] (these systems are considered complete sample-measuring polarimeters [16] for their ability to fully determine the backscatter matrix). Since preferential orientation can be detected through evaluation of the magnitudes of off-diagonal elements of the backscatter phase matrix, these systems can provide information regarding the presence of oriented particles. However, for the measurement of a scattering matrix it is necessary to vary polarization states of both sounding beam and analyzers, which is commonly achieved by means of rotating retarders [21]. The scattering matrix from these measurements is thus determined by combining signals acquired at different sampling times. The results are consequently only reliable if the probed sample is temporally sufficiently stable. Validity of this assumption is clearly questionable in the light of inherent temporal and spatial variability of composition and characteristics of atmospheric aerosols. Variation of the retardances with rotation angle may produce additional systematic error, and spatial and temporal resolutions are limited by the maximum rotation speeds to maintain well-controlled alignment of retarders.

As an alternative to these Mueller polarimeters, we investigate a polarization lidar setup with stationary, standard optical components in this study. The conceptualized system is free of moving parts and therefore more robust, and permits faster sampling rates than conventional Mueller polarimeters. It is, however, an incomplete sample-measuring polarimeter that provides information only for a subset of backscatter matrix elements. This solution is still adequate for approximate characterization of the probed volume, and in addition has the potential of providing data with increased spatial and temporal resolution. This new concept can thus be placed between the afore-mentioned complete Mueller polarimeters and Stokes polarimeters. Accepting partial information on the backscatter phase matrix enables reduction of the instrument complexity that translates to increased reliability, which is particularly important for applications in extreme environments such as the Arctic region. Application of high-quality lasers, detectors and data acquisition equipment with the outlined system enables measurements with higher spatial and temporal resolution than polarimeters with rotating optical components. Absence of moving parts facilitates processing of detected signals because of the less-demanding need for component modeling to properly account for imperfections and angular alignment uncertainties. The design concept of the instrument features simultaneous measurement of all pieces of information that are used in the data inversion. This eliminates uncertainties associated with temporal variabilities in the probed aerosol, and facilitates application of advanced denoising approaches to the recorded data stream.

In this theoretical study, we explore the feasibility of such a polarization lidar system for the measurement of the degree of preferential orientation, depolarization ratio, and backscatter coefficient. Specifically, our focus lies on theoretical development of configurations that exhibit optimal measurement stability when the polarization state of the incident probe beam is held fixed. For the development, we first discuss the general structure of the backscatter phase matrix and establish combinations of matrix elements suitable for indication of preferential orientation. We then determine the configuration of a four-channel system with either a linearly or a circularly polarized incident beam that measures the desired quantities with minimum uncertainties. Finally, the expected performance of the optimum configuration is compared with the performance of traditional two-channel systems for measurement of depolarization ratios and backscatter coefficients. The capabilities of detecting preferential orientation are discussed on the basis of an aerosol consisting of prolate ellipsoidal particles with optical properties of typical atmospheric inorganic dust.

2. Theoretical Background

The assumption that the probed volume contains a large number of randomly oriented particles is valid in many practical situations, but may not be completely justified when ice crystal and other nonspherical hydrometeors and dust are present.

While for large preferentially oriented particles the effect on the measured depolarization ratio may be strong enough for discrimination, it becomes increasingly difficult to detect preferential orientation with conventional techniques when the number of particles or their size decreases. With the aim of improving the capabilities for detection of preferential orientation, we explore the feasibility of measuring some of the off-diagonal elements (or combinations thereof) of the backscatter phase matrix that vanish when the probed aerosol consists of fully randomly oriented particulates. Statistically significant nonzero values in these off-diagonal elements should thus reliably indicate preferential orientation.

Light scattering characteristics of an individual particle is commonly described with the 4×4 scattering phase matrix $\mathbf{Z}$, which transforms the Stokes vector of incident light $\mathbf{S}_{inc} = (I, Q, U, V)^t_{inc}$ to that of the scattered light $\mathbf{S}_{sca}$ (we define all vectors as column vectors and use ^{t} to indicate transposition). For an ensemble of randomly positioned, independently scattering particulates, the ensemble-averaged scattering phase matrix is given by the superposition of individual scattering phase matrices, *i.e.* $\langle \mathbf{Z} \rangle = \sum_{n=1}^{N} \mathbf{Z}_n$. For single scattering in the exact backward direction, the phase matrix of an individual particle in fixed orientation is composed of nine independent elements [22]:

$$\mathbf{Z} = \begin{pmatrix} Z_{11} & Z_{12} & Z_{13} & Z_{14} \\ Z_{12} & Z_{22} & Z_{23} & Z_{24} \\ -Z_{13} & -Z_{23} & Z_{33} & Z_{34} \\ Z_{14} & Z_{24} & -Z_{34} & Z_{44} \end{pmatrix}, \qquad (1)$$

with $Z_{11} - Z_{22} + Z_{33} - Z_{44} = 0$. For a collection of indefinitely many, randomly oriented particles of arbitrary shapes, the scattering matrix simplifies to [22]

$$\mathbf{Z} = \begin{pmatrix} Z_{11} & 0 & 0 & Z_{14} \\ 0 & Z_{22} & 0 & 0 \\ 0 & 0 & -Z_{22} & 0 \\ Z_{14} & 0 & 0 & Z_{44} \end{pmatrix}, \qquad (2)$$

where in general $0 \le Z_{22} \le Z_{11}$, $Z_{44} = Z_{11} - 2Z_{22}$, and $Z_{22} - Z_{11} \le Z_{14} \le Z_{11} - Z_{22}$. If each particle has a plane of symmetry, $Z_{14} = 0$; in addition, for homogeneous, optically inactive, spherical particles $Z_{11} = Z_{22} = -Z_{44}$ [22]. Comparison of Eqs. (1) and (2) clearly reveals that the key to sensitive detection of preferentially oriented particles lies in the analysis of off-diagonal elements other than Z_{14}. Although the gas background may contribute significantly to the diagonal elements of the overall ensemble-averaged scattering matrix $\langle \mathbf{Z} \rangle$, this contribution can be subtracted using complementary Raman-lidar measurements, for instance [1]. But regardless of the background correction, nonzero ratios of off-diagonal elements to Z_{11} indicate preferential orientation (the strength of the indication certainly improves, however, when contributions from randomly oriented scatters (such as the gas molecules) are subtracted). The effect of molecular backscattering is therefore not considered in the following development.

2.1. Structural dependence of backscatter phase matrix on orientation angles

For the choice of an appropriate lidar configuration it is instructive to examine the orientation dependence of the backscatter matrix for axisymmetric particles, which in many cases approximate reasonably well the shape of solid particulates or aerodynamically distorted water droplets. As an example of an axisymmetric particle, we use a prolate ellipsoidal particle. The particle is assumed to be located in the origin of a lab coordinate system whose z-axis is aligned with the propagation direction of the incident light. Adopting Mishchenko's definitions [23], we assume the z'-axis of the particle coordinate system is aligned with the particle symmetry axis (see Fig. 1). The angle $\beta \ni [0, 180°]$ then measures the angle between propagation direction and the particle symmetry axis; $\alpha \ni [0, 360°)$ specifies the rotation angle about the z-axis such that for $\alpha = 0$ the particle symmetry axis lies in the xz-plane of the lab coordinate system (the third Euler angle, γ, has no significance for axisymmetric particles and is set equal to zero). According to the analysis by Hu *et al.* [24], axisymmetric particles fall into Class ($\bar{A}$). The symmetry properties of any scatterer in that class manifest themselves through regularities in the backscatter phase matrix with respect to the azimuthal orientation angle α: Z_{12} and Z_{34} are proportional to $\cos 2\alpha$, Z_{13} and Z_{24} to $\sin 2\alpha$, and Z_{23} to $\sin 4\alpha$, with proportionality constants dependent on the polar angle β. Z_{11} and Z_{44} are independent of α, whereas Z_{22} and Z_{33} have α-independent components with superimposed $\cos 4\alpha$ components. The overall magnitudes of the matrix elements are functions of the polar angle β, particle size and the refractive index. As an example, Fig. 2 shows the orientation dependence of the backscatter phase matrix element Z_{11} and the other independent elements Z_{ij} relative to Z_{11} for a prolate ellipsoid with an aspect ratio of $2:1$ ($Z_{14} = Z_{41} = 0$ for particles in this class and is therefore omitted in Fig. 2).

Fig. 2 illustrates the sine-cosine dependences with respect to the azimuthal angle α, but also shows the range in magnitude of the backscatter coefficient Z_{11}. While independent from α, Z_{11} varies over more than two orders of magnitude over the entire

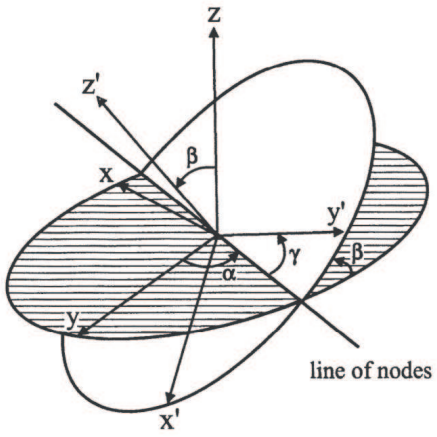

Figure 1: Euler angles of rotation α, β, and γ. Laboratory reference frame: $\{x, y, z\}$; particle reference frame: $\{x', y', z'\}$. Reproduction of Fig. 2 in [23].

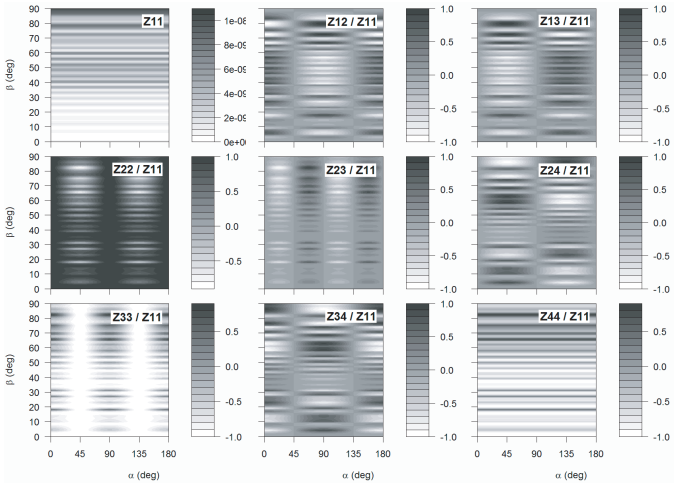

Figure 2: Backscatter phase matrix elements relative to Z_{11} (in cm^2/sr) as a function of the azimuthal (α) and polar (β) orientation angles for a prolate ellipsoid with aspect ratio 2 : 1 and a major axis size parameter $x_b = 2\pi b/\lambda = 49.6$. This size parameter corresponds to a 10 μm long particle illuminated with visible light at 632.8 nm wavelength. The particle refractive index is $m = 1.53 + i0.008$, which is a typical value for mineral dust particles in the atmosphere; the refractive index of the surrounding medium (air) is set to 1.0. The calculations were performed using the extended-precision T-matrix code by Mishchenko *et al.* [25–27], downloaded from [28]. The angular resolution $\Delta\alpha = \Delta\beta = 1^\circ$; $Z_{ij}\,(180^\circ < \alpha < 360^\circ, 90^\circ < \beta \leq 180^\circ) = Z_{ij}\,(\alpha - 180^\circ, 180^\circ - \beta)$ due to the particle symmetry.

range of polar angles β. This translates to a root-mean-square (rms)-deviation of the backscattering coefficient $Z_{11}(\alpha,\beta)$ from the value for randomly oriented particles $\langle Z_{11}\rangle$ of about 67% ($rms^2 = \int_0^{2\pi}\int_0^{\pi}[Z_{11}(\alpha,\beta) - \langle Z_{11}\rangle]^2 \sin\beta\,\mathrm{d}\beta\mathrm{d}\alpha/4\pi$). This large orientation-averaged rms value indicates that there is a potential for massive over- or underestimation of the amount of particles if the particles are predominantly aligned in a particular direction. As shown in Fig. 2, off-diagonal elements can assume absolute values as large as the backscatter coefficient Z_{11}. Analysis for axisymmetric particles with large absorption coefficient (such as black carbon or soot [29]), reveals that the structure of the backscatter phase matrix is similar, but that the maximum absolute values of the off-diagonal elements are considerably smaller (less than 10%) than Z_{11} (results not shown here). The inherent zero-crossings of off-diagonal elements at some α-β combinations suggest that linear combinations of off-diagonal elements produce zero values in some situations of preferential orientation, thus falsely indicating randomness in the particle orientation. It appears reasonable to combine off-diagonal elements that are phase-shifted with respect to α, such as Z_{12} or Z_{34} with Z_{13} or with Z_{24}, to increase the rate of correct indication of preferential orientation, but there is no real advantage of one over the other combination. Configurations in which Z_{14} combines with one of the diagonal elements, on the other hand, seem beneficial since many types of atmospheric particles have a symmetry plane according to Class ($\bar{A}$) [24]. As $Z_{14} = 0$ for that symmetry class, the element that is combined with Z_{14} is determined with little systematic error.

2.2. Signal models and instrument matrix

For the development of a suitable configuration, we assume a setup with a fully polarized incident beam with either linear ("L-setup") or a circular polarization ("C-setup"), similar to the time-proven configuration of conventional polarization lidar setups. According to [18], polarization states are preserved during transmission even through relatively dense clouds, *i.e.* using the scalar radiative transfer equation to represent the propagation of incident and scattered light through the atmosphere is a valid approximation. The optimum configurations are determined from the relative magnitudes of the signals in the four channels, expressed as comparable differential cross-sections y_i. We assume that the lidar return light is collected with a single telescope and subsequently split into four beams for analysis, such that signal ratios become independent of range-dependent geometry factors. The optical trains for detection of the backscattered light are assumed to consist of beam splitters, linear polarizers, and optional quarter-wave plates, as well as bandpass filters, mirrors, fast detectors and electronic data acquisition systems. We assume each of the four sub-beams passes an optional quarter-wave plate and a linear polarizer before arriving at the detector face. The system thus employs four analyzer states to provide four independent measurements for characterization of the probed aerosol.

The attenuation-corrected differential cross sections y_i (in m^2/sr) in each of the four analyzer channels $i = 1,\ldots,4$ are given by

$$y_i = \mathbf{e}^t\,\mathbf{P}_i\,\mathbf{Q}_i\,\mathbf{Z}\,\mathbf{I}_{inc}\ , \qquad (3)$$

where y_i is the measured voltage divided by the respective calibration constant, $\mathbf{e} = (1,0,0,0)^t$ selects the first component of the Stokes vector (which is the only one directly measurable by a detector), $\mathbf{P}_i$ is the Mueller matrix for the linear polarizer, $\mathbf{Q}_i$ is the Mueller matrix for the quarter-wave plate. Assuming a fixed reference plane defined by the direction of the propagating laser beam and the electric field vector of the linear polarized laser output (the field vector is parallel to the reference plane), the normalized Stokes vectors are given by $\mathbf{I}_{L,inc} = (1,1,0,0)^t$ or $\mathbf{I}_{C,inc} = (1,0,0,1)^t$ for L- and C-setups, respectively.

For establishing the best configuration, ideal components and complete polarization of the probe beam are assumed. The Mueller matrix $\mathbf{P}_i = \mathbf{P}(\chi_i)$ for the linear polarizer with the transmission axis at an angle χ relative to the reference plane is defined in [30]. The polarizer passes field components parallel or perpendicular to the reference plane if $\chi = 0$ or $\chi = 90^\circ$, respectively. The quarter-wave plate is modeled as an ideal retarder with retardance δ_i and with the fast axis angle ζ_i relative to the reference plane. The Mueller matrix of an ideal retarder $\mathbf{Q}_i = \mathbf{Q}(\delta_i,\zeta_i)$ can be found in [30]. The retardance for a quarter-wave plate equals $\delta = 90^\circ$; for detection channels without a quarter-wave plate, $\delta = 0^\circ$.

With eq. (3) and the elements of the backscatter phase matrix $\mathbf{Z}$ arranged into a vector $\mathbf{z} = (Z_{11}, Z_{12}, Z_{13}, Z_{14}, Z_{22}, Z_{23}, Z_{24}, Z_{33}, Z_{34}, Z_{44})^t$ [21], the measured light intensities $y_{L,i}$ for the L-setup, $\mathbf{I}_{L,inc} = (1,1,0,0)^t$, are expressed in matrix form as

$$y_{L,i} = \frac{1}{2}\,(1, 1+a_i, b_i, d_i, a_i, b_i, d_i, 0, 0, 0)\cdot\ \mathbf{z} = \mathbf{x}^t_{z,L,i}\,\mathbf{z} \qquad (4)$$

where

$$a_i = \cos 2\chi_i + (1 - \cos\delta_i)\sin 2\zeta_i \sin 2(\chi_i - \zeta_i)$$
$$b_i = -\cos\delta_i \sin 2\chi_i - (1 - \cos\delta_i)\sin 2\zeta_i \cos 2(\chi_i - \zeta_i)$$
$$d_i = \sin\delta_i \sin 2(\chi_i - \zeta_i)$$

Examination of the measurement vector $\mathbf{x}_{z,L,i}$ in eq. (4) reveals that Z_{33}, Z_{34}, and Z_{44} cannot be determined since no combination of retardance, fast axis angle and polarizer angle will result in signal contributions from these elements. Moreover, elements Z_{14} and Z_{24} cannot be distinguished because for any choice of δ_i, ζ_i and χ_i the two elements contribute equally to the measured intensity. The same is true for elements Z_{13} and Z_{23}. Elements Z_{11}, Z_{12} and Z_{22} are linearly linked and any combination $(\delta_i, \zeta_i, \chi_i)$ provides information for only two out of the three. A configuration with four or more detection lines, each of which consisting of a linear retarder and a polarizer, and a linearly polarized probe beam thus enables determination of at most four independent pieces of information. In our four-channel configuration the four independent pieces of information, denoted as parameter vector $\boldsymbol{\xi}_L$, are fully resolved. $\boldsymbol{\xi}_L$ is naturally defined, based on the analysis above, as

$$\boldsymbol{\xi}_L = \begin{pmatrix} \xi_{L,1} \\ \xi_{L,2} \\ \xi_{L,3} \\ \xi_{L,4} \end{pmatrix} = \begin{pmatrix} Z_{11} + Z_{12} \\ Z_{12} + Z_{22} \\ Z_{13} + Z_{23} \\ Z_{14} + Z_{24} \end{pmatrix} . \tag{5}$$

The equation for the detected intensity in the i-th channel, eq. (4), can thus be rewritten as

$$y_{L,i} = \frac{1}{2}(1, a_i, b_i, d_i) \cdot \boldsymbol{\xi}_L = \mathbf{x}^t_{\xi,L,i}\, \boldsymbol{\xi}_L \, . \tag{6}$$

The measurement matrix $\mathbf{X}_L$ for the four-channel system, which relates the vector of the combination parameters $\boldsymbol{\xi}_L$ to the vector of measured intensities $\mathbf{y}_L = (y_{L,1}, \ldots, y_{L,4})^t$, is compiled from the row vectors $\mathbf{x}^t_{\xi,L,i}$ defined in eq. (6) according to

$$\mathbf{y}_L = \begin{pmatrix} \mathbf{x}^t_{\xi,L,1} \\ \mathbf{x}^t_{\xi,L,2} \\ \mathbf{x}^t_{\xi,L,3} \\ \mathbf{x}^t_{\xi,L,4} \end{pmatrix} \boldsymbol{\xi}_L = \mathbf{X}_L\, \boldsymbol{\xi}_L \, . \tag{7}$$

The conventional two-channel system with $\{\delta, \zeta, \chi\}_1 = \{0°, 0°, 0°\}$ and $\{\delta, \zeta, \chi\}_2 = \{0°, 0°, 90°\}$ yields, according to eq. (4), $\mathbf{x}_{z,L,1} \propto (1, 2, 0, 0, 1, 0, 0, 0, 0, 0)^t$ and $\mathbf{x}_{z,L,2} \propto (1, 0, 0, 0, -1, 0, 0, 0, 0, 0)^t$. This gives the linear depolarization ratio $\delta_L = y_{L,2}/y_{L,1} = (Z_{11} - Z_{22})/(Z_{11} + 2Z_{12} + Z_{22})$ or $d_L = y_{L,2}/(y_{L,1} + y_{L,2}) = (Z_{11} - Z_{22})/2(Z_{11} + Z_{12})$ [31]. If the probed aerosol truly consists of randomly oriented particles ($Z_{12} = 0$), both backscatter cross section Z_{11} and element Z_{22} can be determined correctly, otherwise Z_{11} and Z_{22} are biased. With the chosen parametrization for $\boldsymbol{\xi}_L$, the depolarization ratios follow as $\delta_L = (\xi_{L,1} - \xi_{L,2})/(\xi_{L,1} + \xi_{L,2})$ and $d_L = (1 - \xi_{L,2}/\xi_{L,1})/2$, which shows that the measured, combined parameters $\boldsymbol{\xi}_L$ can be easily transformed into the traditional depolarization ratios.

For the C-setup, $\mathbf{I}_{C,inc} = (1, 0, 0, 1)^t$, the configuration vector is different, but structurally similar. Now, the measured light intensities $y_{C,i}$ are given by

$$y_{C,i} = \frac{1}{2}(1, a_i, b_i, 1 + d_i, 0, 0, a_i, 0, -b_i, d_i) \cdot \mathbf{z} = \mathbf{x}^t_{z,C,i}\, \mathbf{z} \tag{8}$$

with a_i, b_i, and d_i as defined earlier.

By examining the measurement vectors $\mathbf{x}_{z,C,i}$ in eq. (8) it can be concluded that Z_{22}, Z_{23}, and Z_{33} cannot be determined and elements Z_{12} and Z_{24}, as well as Z_{13} and Z_{34} are indistinguishable. As for the L-setup, at most four independent parameters can be determined, regardless of the number different detection lines. To determine the full parameter vector $\boldsymbol{\xi}_C$ defined as

$$\boldsymbol{\xi}_C = \begin{pmatrix} \xi_{C,1} \\ \xi_{C,2} \\ \xi_{C,3} \\ \xi_{C,4} \end{pmatrix} = \begin{pmatrix} Z_{11} + Z_{14} \\ Z_{12} + Z_{24} \\ Z_{13} - Z_{34} \\ Z_{14} + Z_{44} \end{pmatrix} \tag{9}$$

we again use four detection lines, specified through $i = 1, \ldots, 4$. The detected intensity in the i-th channel follows from eqs. (8) and (9):

$$y_{C,i} = \frac{1}{2}(1, a_i, b_i, d_i) \cdot \boldsymbol{\xi}_C = \mathbf{x}^t_{\xi,C,i}\, \boldsymbol{\xi}_C \tag{10}$$

Similar to eq. (7), the vector of measured intensities $\mathbf{y}_C = (y_{C,1}, \ldots, y_{C,4})^t = \mathbf{X}_C\, \boldsymbol{\xi}_C$, with the row vectors $\mathbf{x}^t_{\xi,C,i}$ (eq. (10)) stacked to obtain the measurement matrix $\mathbf{X}_C$. By comparing eqs. (10) and (6) one can easily see that $\mathbf{X}_L = \mathbf{X}_C$. With this, the task of finding an optimal configuration as discussed below simplifies since best-possible performance for both system configurations is achieved with the same set of parameters $\{\delta, \zeta, \chi\}_{i=1,\ldots,4}$.

The conventional two-channel system with $\{\delta, \zeta, \chi\}_1 = \{90°, 90°, -45°\}$ and $\{\delta, \zeta, \chi\}_2 = \{90°, 90°, 45°\}$ results in $\mathbf{x}_{z,C,1} \propto (1, 0, 0, 0, 0, 0, 0, 0, 0, -1)^t$ and $\mathbf{x}_{z,C,2} \propto (1, 0, 0, 2, 0, 0, 0, 0, 0, 1)^t$. This gives the circular depolarization ratio $\delta_C = y_{C,2}/y_{C,1} = (Z_{11} + 2Z_{14} + Z_{44})/(Z_{11} - Z_{44})$ or $d_C = y_{C,2}/(y_{C,1} + y_{C,2}) = (Z_{11} + 2Z_{14} + Z_{44})/2(Z_{11} + Z_{14})$ [31]. Due to $Z_{14} \neq 0$ also for randomly oriented particulates, both elements Z_{11} and Z_{44} are biased unless the aerosol consists of Class($\bar{A}$)-symmetric particles [24]. With the chosen parametrization for $\boldsymbol{\xi}_C$, the depolarization ratios follow as $\delta_C = (\xi_{C,1} + \xi_{C,4})/(\xi_{C,1} - \xi_{C,4})$ and $d_C = (1 + \xi_{C,4}/\xi_{C,1})/2$. As before, simple manipulation enables direct comparison with traditional polarization lidar results. Direct interpretation of the $y_{C,i}$ and $y_{L,i}$ is, however, complicated as the measured signals are linear combinations of several components of $\boldsymbol{\xi}_C$ or $\boldsymbol{\xi}_L$.

3. Optimum system configuration

For the system design, specified in terms of the parameters $\{\delta, \zeta, \chi\}_{i=1,\ldots,4}$, we use the ratio between the largest and the smallest singular values of the measurement matrix $\mathbf{X}$ as the criterion for the optimization of Mueller matrix polarimeters [21]. Singular Value Decomposition (SVD) of $\mathbf{X}$ yields $\mathbf{X} = \mathbf{U}\mathbf{D}\mathbf{V}^t$, where $\mathbf{U}$ and $\mathbf{V}$ are orthonormal matrices and $\mathbf{D} = \mathrm{diag}(\mu_1, \ldots \mu_4)$

is a diagonal matrix with the singular values of $\mathbf{X}$ as the diagonal elements. If the measured cross-sections $\mathbf{y} = \mathbf{X}\boldsymbol{\xi}$ contain additive, independent, identically distributed noise with variance σ^2, *i.e.* the covariance matrix $\boldsymbol{\Sigma}_\mathbf{y} = \sigma^2 \mathrm{diag}(1,1,1,1)$, then the covariance matrix of the desired quantities $\hat{\boldsymbol{\xi}} = \mathbf{X}^{-1}\mathbf{y}$ follows as $\boldsymbol{\Sigma}_{\hat{\boldsymbol{\xi}}} = \mathbf{X}^{-1}\boldsymbol{\Sigma}_\mathbf{y}\mathbf{X}^{-t} = \sigma^2(\mathbf{X}^t\mathbf{X})^{-1}$ [32] (the $\hat{}$ is used to distinguish noisy estimates from the true, underlying quantities). With the SVD of $\mathbf{X}$ this expression simplifies to $\boldsymbol{\Sigma}_{\hat{\boldsymbol{\xi}}} = \sigma^2\mathbf{V}\mathbf{D}^{-2}\mathbf{V}^t = \mathbf{V}\boldsymbol{\Lambda}\mathbf{V}^t$, which is the eigendecomposition of $\boldsymbol{\Sigma}_{\hat{\boldsymbol{\xi}}}$ with the eigenmatrix $\boldsymbol{\Lambda} = \mathrm{diag}(\sigma^2/\mu_1^2, \ldots, \sigma^2/\mu_4^2)$. The ratio of singular values measures the degree of singularity of $\mathbf{X}$ (smaller ratios are the indicators for lower degree of singularity, or good conditioning [33]), and also relates to the amplification of noise in the signal inversion (a well-conditioned design matrix is as far as possible from being singular and thus results in a balanced distribution of noise over the derived quantities). In order to determine the four unknown quantities $\xi_1, ..., \xi_4$ with our four-channel system, the 4×4 matrix $\mathbf{X}$ must be full rank, which implies that all four singular values must be non-zero.

The optimum configuration parameter vector $\{\delta, \zeta, \chi\}_{i=1,\ldots,4}$ was determined numerically using a genetic algorithm [34], followed by a deterministic optimization routine [35], both part of the R-code software package [36]. The first step was to find the smallest possible ratio of singular values by varying all 12 components of the configuration parameter vector in the ranges $0° \le \delta_i \le 180°$, $0° \le \zeta_i \le 90°$, and $0° \le \chi_i \le 90°$. Several independent runs of the genetic algorithm converged to the one and the same optimum of $\mu_{max}/\mu_{min} = \sqrt{3}$, suggesting that the algorithm parameters (population size, number of generation, probabilities for mutation and cross-over, etc. [34]) were chosen adequately. In the second step, the search space for the configuration parameters was increasingly constrained by reducing the number of varied configuration parameters until the singular value ratio $\sqrt{3}$ could not be achieved any longer. The remaining parameters were fixed at convenient values (0° for the angles of the fast axis orientation ζ_i, 0° or 90° for the retardances δ_i). The optimum configuration for four detection channels from this procedure is given by

$$\begin{aligned} \{\delta,\zeta,\chi\}_1 &= \{0°, 0°, \gamma\} \\ \{\delta,\zeta,\chi\}_2 &= \{0°, 0°, -\gamma\} \\ \{\delta,\zeta,\chi\}_3 &= \{90°, 0°, 90° - \gamma\} \\ \{\delta,\zeta,\chi\}_4 &= \{90°, 0°, -(90° - \gamma)\} \end{aligned} \qquad (11)$$

where $\gamma = (1/2)\arccos(1/\sqrt{3}) = 27.37°$. Detection lines 1 and 2 thus consist of only linear polarizers with the transmission axis at an angle of ±27.37° with respect to the reference plane; each of the detection lines 3 and 4 have a quarter-wave plate with the fast axis aligned parallel to the reference plane and a linear polarizer with a polarization angle ±62.63° relative to the reference plane. The four-channel system can thus be viewed as a combination of the two conventional polarization lidar systems, but with different polarizer angles to access off-diagonal elements of the backscatter phase matrix.

The schematic shown in Fig. 3 is an example of an optical train of the analyser side for both setups. The overall instrumentation is envisioned to be similar to conventional polarization lidar systems. The generator side involves separate conditioning of the pulsed laser beam to produce the desired polarization state, beam expansion to reduce beam divergence, and steering of the beam to align it with the optical axis of the receiver telescope. The analyser side consists of a telescope, optical components as shown in Fig. 3, detectors (photon counters or photomultiplier tubes), and electronics to simultaneously record the signals in the four analyser channels and an optional channel to monitor the intensity of the laser beam. A conventional two-channel polarization lidar system can thus be upgraded in a straight-forward manner. Placing the four polarizer angles as specified in eq. (11) and calibrating the detection side is somewhat more complicated, but could be based on Rayleigh-scattering from a gas with known scattering cross section [30] to minimize systematic errors. As discussed in more detail below, the measured signals follow trigonometric relationships with respect to the polarizer angle, which may be utilized in that procedure.

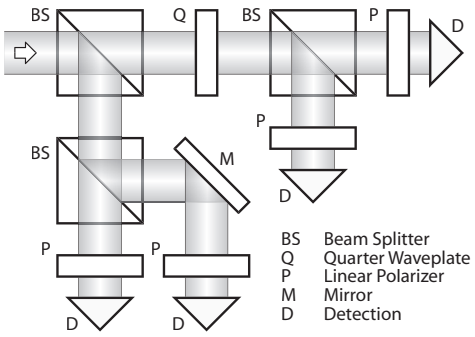

Figure 3: Schematic of an optimum four-channel polarization lidar system.

Examination of eq. (11) shows that the optimum configuration is represented by a single characteristic angle γ defining all four polarizer angles $\chi_1, \ldots, \chi_4$. With the waveplate retardances and orientation given in eq. (11), the measurement matrix $\mathbf{X}$ for both configurations is given by

$$\mathbf{X} = \frac{1}{2}\begin{pmatrix} 1 & \cos 2\gamma & -\sin 2\gamma & 0 \\ 1 & \cos 2\gamma & \sin 2\gamma & 0 \\ 1 & -\cos 2\gamma & 0 & \sin 2\gamma \\ 1 & -\cos 2\gamma & 0 & -\sin 2\gamma \end{pmatrix}. \qquad (12)$$

For statistically independent measured cross-sections $\mathbf{y}$ with equal variances the covariance matrix $\boldsymbol{\Sigma}_\mathbf{y} = \sigma^2\mathrm{diag}(1,1,1,1)$, which yields the diagonal covariance matrix

$$\boldsymbol{\Sigma}_{\hat{\boldsymbol{\xi}}} = \sigma^2 \mathrm{diag}\left(1, \frac{1}{\cos^2 2\gamma}, \frac{2}{\sin^2 2\gamma}, \frac{2}{\sin^2 2\gamma}\right). \qquad (13)$$

In this case, the noise variances in the calculated ξ_3 and ξ_4 are equal regardless of γ. For the optimal γ, which yields highest possible fidelity in all four derived quantities, the variances of ξ_2, ξ_3, and ξ_4 coincide.

For an ideal photon counting system for light detection, the observed counting noise is proportional to the detected radiant

flux, *i.e.* $\sigma_i^2 \propto y_i$. Assuming channel-independent transmission characteristic, the covariance matrix $\mathbf{\Sigma_y} = K\mathrm{diag}(y_1, \ldots, y_4)$. Using $\mathbf{y} = \mathbf{X}\boldsymbol{\xi}$ gives

$$\mathbf{\Sigma}_{\boldsymbol{\xi},sh} = \frac{K\xi_1}{2}\begin{pmatrix} 1 & (\xi_2/\xi_1) & (\xi_3/\xi_1) & (\xi_4/\xi_1) \\ (\xi_2/\xi_1) & \frac{1}{\cos^2 2\gamma} & \frac{(\xi_3/\xi_1)}{\cos 2\gamma} & -\frac{(\xi_4/\xi_1)}{\cos 2\gamma} \\ (\xi_3/\xi_1) & \frac{(\xi_3/\xi_1)}{\cos 2\gamma} & \frac{2+2(\xi_2/\xi_1)\cos 2\gamma}{\sin^2 2\gamma} & 0 \\ (\xi_4/\xi_1) & -\frac{(\xi_4/\xi_1)}{\cos 2\gamma} & 0 & \frac{2-2(\xi_2/\xi_1)\cos 2\gamma}{\sin^2 2\gamma} \end{pmatrix} \tag{14}$$

In this case, correlations can be avoided only if ξ_2, ξ_3 and ξ_4 are equal to zero (*i.e.* randomly oriented particles with $\delta_L = 1$ or $\delta_C = 1$ for the *L*- and *C*-setup, respectively). It is worth noting that the variances in the calculated ξ's are determined by ξ_1 and ξ_2, apart from γ. For the *L*-configuration, in which ξ_2 assumes nonzero values also for randomly oriented values, the uncertainties in the determined orientation markers ξ_3 and ξ_4 are dependent on the depolarization characteristics of the probed volume. In contrast, with circular polarized light, the variances of all four calculated ξ's are only proportional to ξ_1 when probing randomly oriented particulates (since $\xi_2 = 0$). This polarization-insensitivity suggests that the *C*-setup is superior with respect to the noise transmission characteristics.

Fig. 3 illustrates the sensitivity of expected uncertainties according to eqs. (13) and (14) as a function of the angle γ for the two limit noise conditions discussed (assuming $\sigma^2 = K\xi_1/2 = 1$). As clearly seen, the optimum γ is given by the intersection of the curves for the standard deviations $\sigma(\xi_2), \ldots, \sigma(\xi_4)$ for signal-independent measurement noise ($\sigma = $ const.). For the photon-counting case $\sigma(\xi_3)$ and $\sigma(\xi_4)$ increasingly deviate from the thick lines for $\sigma = $ const. with increasing ξ_2/ξ_1. The optimum γ, corresponding now to the intersection of the curves for $\sigma(\xi_2)$ and for the larger of $\sigma(\xi_3)$ and $\sigma(\xi_4)$, is therefore slightly larger (e.g. $\gamma_{\mathrm{opt}} = 30°$ for $\xi_2/\xi_1 = \pm 1$). However, the increased uncertainty when using $\gamma = 27.4°$ is small, justifying the optimization approach followed. Fig. 3 also shows that with $\gamma = 0$ and $\gamma = 45°$, which represent the conventional system configurations, $\xi_{3,4}$ or ξ_2 cannot be determined (as indicated by enormous standard deviations).

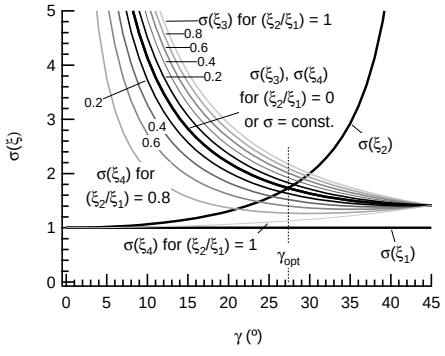

Figure 4: Distribution of measurement noise in calculated quantities $\xi_1, \ldots, \xi_4$ in dependence of the design angle γ for uncorrelated measurement noise with (a) equal, variance $\sigma^2(y_i) = \sigma^2$, and (b) signal-proportional variance $\sigma^2(y_i) = y_i(\gamma)$ for typical ratios ξ_2/ξ_1.

For both operation modes (linearly polarized parallel and right-circularly polarized incident light) the optimum design matrix equals

$$\mathbf{X} = \frac{1}{2}\begin{pmatrix} 1 & 1/\sqrt{3} & -\sqrt{2}/\sqrt{3} & 0 \\ 1 & 1/\sqrt{3} & \sqrt{2}/\sqrt{3} & 0 \\ 1 & -1/\sqrt{3} & 0 & \sqrt{2}/\sqrt{3} \\ 1 & -1/\sqrt{3} & 0 & -\sqrt{2}/\sqrt{3} \end{pmatrix}. \tag{15}$$

Interestingly, the four vectors $\mathbf{v}_i$ formed from the i-th row vector of $\mathbf{X}$ such that $\mathbf{v}_i = (X_{i,2}, X_{i,3}, X_{i,4})^t$ span a regular tetrahedron, a result obtained also by Azzam [37] for the optimum configuration of a quite different four-detector polarimeter. The inverse of the design matrix for conversion of the measured intensities $\mathbf{y}$ to produce estimates of the unknowns

$$\hat{\boldsymbol{\xi}} = \mathbf{X}^{-1}\,\mathbf{y} \tag{16}$$

follows as

$$\mathbf{X}^{-1} = \frac{1}{2}\begin{pmatrix} 1 & 1 & 1 & 1 \\ \sqrt{3} & \sqrt{3} & -\sqrt{3} & -\sqrt{3} \\ -\sqrt{6} & \sqrt{6} & 0 & 0 \\ 0 & 0 & \sqrt{6} & -\sqrt{6} \end{pmatrix}, \tag{17}$$

which, for the case of independent, identically distributed measurement noise of variance σ^2, yields $\mathbf{\Sigma}_{\boldsymbol{\xi}} = \sigma^2\mathrm{diag}(1,3,3,3)$ (see eq. (13). For an ideal shot-noise limited system, $\mathbf{\Sigma}_{\boldsymbol{\xi},sh}$ follows from eq. (14) as

$$\mathbf{\Sigma}_{\boldsymbol{\xi},sh} = \frac{K}{2}\begin{pmatrix} \xi_1 & \xi_2 & \xi_3 & \xi_4 \\ \xi_2 & 3\xi_1 & \sqrt{3}\xi_3 & -\sqrt{3}\xi_4 \\ \xi_3 & \sqrt{3}\xi_3 & 3\xi_1 + \sqrt{3}\xi_2 & 0 \\ \xi_4 & -\sqrt{3}\xi_4 & 0 & 3\xi_1 - \sqrt{3}\xi_2 \end{pmatrix}. \tag{18}$$

For conventional systems, for which the design matrices are given by

$$\mathbf{X}_L = \frac{1}{2}\begin{pmatrix} 1 & 1 \\ 1 & -1 \end{pmatrix}; \quad \mathbf{X}_C = \frac{1}{2}\begin{pmatrix} 1 & -1 \\ 1 & 1 \end{pmatrix}, \tag{19}$$

the corresponding covariance matrices are also diagonal, but uncertainties are distributed differently: $\mathbf{\Sigma}_{\boldsymbol{\xi},conv} = \sigma^2\mathrm{diag}(2,2)$. This suggests that, for comparable random error in the measured signals, the first combination element ξ_1 (either $\xi_1 = Z_{11} + Z_{12}$ or $\xi_1 = Z_{11} + Z_{14}$ for both conventional and alternative systems) can be determined more accurately with the proposed four-channel systems. The variance in the second combination element $\xi_2 = (Z_{12} + Z_{22})$ or $\xi_4 = (Z_{14} + Z_{44})$, in contrast, is 50% higher. Consequently, the proposed system appears to have similar overall performance characteristics as the traditional systems. This analysis, however, neglects the fact that individual channels may have different levels of electronic noise and photon-shot noise. The latter is associated with the finite number of detected photons in photomultiplier tubes or other photon-counting devices. Its variance is proportional to the mean signal and becomes dominant when detecting low light intensities (corresponding to small photon fluxes) [38]. A fair comparison must also account for the increased shot noise caused by the additional beam splitter in each proposed alternative system, and the differences in the magnitudes

of the measured signals due to the differences in the polarizer angle settings. It is therefore largely dependent on the probed environment whether the proposed system out-performs a traditional one or not, but undoubtedly it offers the advantage of an extended capability for detection of preferential orientation.

Apart from the full vectors $\boldsymbol{\xi}$, linear combinations of the measured cross-sections may be useful as crude indicators for the presence of preferential orientation. For the system with linear incident polarization $(\xi_{L,3} \pm \xi_{L,4}) = \sqrt{3/2}(-y_{L,1} + y_{L,2} \pm y_{L,3} \mp y_{L,4})$, and for circular polarized incident light, $(\xi_{C,2} \pm \xi_{C,3}) = (\sqrt{3}/2)([1 \mp \sqrt{2}]y_{C,1} + [1 \pm \sqrt{2}]y_{C,2} - y_{C,3} - y_{C,4})$. In both cases, the calculated quantities are uncorrelated with variances $6\sigma^2$ if the y_i's have identical, independent zero-mean noise with variance σ^2.

Finally, a feature different from conventional setups is that all four measured lidar return cross-sections are greater than zero, regardless of the extent of depolarization or preferential particle orientation. As discussed in more detail in the Discussion section, the calculated parameters $\xi_{L,3}$ and $\xi_{L,4}$ (or $\xi_{C,2}$ and $\xi_{C,3}$) provide independent estimates of the amount of noise in the y_i if the probed aerosol is composed of randomly oriented particles. Specifically, the noise variances are estimated as $\hat{\sigma}^2 = (\xi_{L,3}^2 + \xi_{L,4}^2)/6$ or $\hat{\sigma}^2 = (\xi_{C,2}^2 + \xi_{C,3}^2)/6$ if the measured cross-sections contain identical independent zero-mean noise with variance σ^2. With ideal photon-counting detection, $(\xi_{L,3}^2 + \xi_{L,4}^2)/6$ and $(\xi_{C,2}^2 + \xi_{C,3}^2)/6$ give estimates of ξ_1. The two additional measurements thus provide information to assess uncertainties in reported parameters when all particles are randomly oriented.

4. Discussion

To illustrate the performance characteristics of the investigated lidar configurations we present examples of expected signals and retrieved parameters. After some analysis of the uncertainties associated with application of the proposed system as a replacement of the traditional two-channel systems, the application to ultra-short pulse lidar systems is discussed. For simplicity, we assume an artificial aerosol composed of monodisperse mineral particles. The particles have typical refractive index, aspect ratio and size as listed in the caption of Fig. 2. The system performance is evaluated for two cases: (1) all particles are randomly oriented, and (2) 10 % of the particles are aligned in a preferential direction. For both scenarios, the effect of random noise (with signal-independent and signal-proportional variances) on the uncertainties of the retrieved parameters is discussed.

To analyze the uncertainties in the retrieved parameters we consider a generic model for the random variability in the measured cross-sections $\mathbf{y}$ due to detection electronics noise and shot noise. The random variability in the y_i, σ_i^2, is thus expressed as the sum of a signal-independent variance $\sigma_{el,i}^2$ and a signal proportional variance $\sigma_{sh,i}^2 = k_i\mu_i$.

In addition to the random variability, systematic offsets may reduce the quality of the quantities calculated from the measured data. Combined with the random noise, the measured cross-sections can be expressed as $\mathbf{y} = (\mathbf{X} - \boldsymbol{\eta}_\mathbf{X})\boldsymbol{\xi} + \boldsymbol{\eta} + \boldsymbol{\epsilon}$, where $\boldsymbol{\eta}_\mathbf{X}$ represents the difference between true and calibration design matrix, $\boldsymbol{\xi}$ is the underlying vector of unknows describing the probed aerosol, $\boldsymbol{\eta}$ is the direct bias in the measured cross section (typically a function of the underlying true signal), $\boldsymbol{\epsilon}$ represents the zero-mean random measurement noise. Substitution into eq. (16) yields the expectation $\mathrm{E}\hat{\boldsymbol{\xi}} = \boldsymbol{\xi} + \mathbf{X}^{-1}(\boldsymbol{\eta} - \boldsymbol{\eta}_\mathbf{X}\boldsymbol{\xi})$ (the covariance matrix $\boldsymbol{\Sigma}_{\hat{\boldsymbol{\xi}}} = \mathbf{X}^{-1}\boldsymbol{\Sigma}_{\boldsymbol{\epsilon}}\mathbf{X}^{-t}$). The systematic errors in measurements and system parameters thus result in a bias in the estimated parameters $\boldsymbol{\eta}_{\boldsymbol{\xi}} = \mathbf{X}^{-1}(\boldsymbol{\eta} - \boldsymbol{\eta}_\mathbf{X}\boldsymbol{\xi})$. The magnitude of this bias strongly depends on the actual physical implementation of the instrument, and should be evaluated in the quantification of uncertainties of results derived from experimental data. Careful calibration (*i.e.* experimental determination of the design matrix $\mathbf{X}$) and, in certain cases, additional modeling of the optical transfer characteristics are necessary to keep biases at a minimum however. For the discussion of the instrument concept in comparison with conventional systems (which, of course, are also susceptable to systematic errors) detailed analysis of the effects of systematic errors is of secondary importance. In the following analysis we therefore focus on random noise, which in practice can be estimated using statistical methods for time-series analysis (*e.g.* [39]) and ignore systematic errors in measured cross-sections and design matrix. We further concentrate only on an individual sample $\mathbf{y}$ at some arbitrary time, since all information for signal inversion is acquired simultaneously in the four channels.

Uncertainty estimates in derived ratios and functions of $\boldsymbol{\xi}$ are produced by applying the Gauss error propagation formula (also known as Delta Method [40]). Expressed in matrix form, the variance in $g(\boldsymbol{\xi})$ is approximated as $\sigma_g^2 = (\nabla g)^t \boldsymbol{\Sigma}_{\boldsymbol{\xi}} (\nabla g)$, where $\nabla g(\boldsymbol{\xi}) = (\partial g/\partial\xi_1, \ldots, \partial g/\partial\xi_4)^t$. This approximation provides adequate uncertainty estimates if the propagated noise level is sufficiently small. For the sake of the following discussion we assume this assumption is valid, but point out that the obtained uncertainties may be underestimated for largest measurement noise.

4.1. Randomly oriented particles

In this situation, two of the four retrieved quantities $\boldsymbol{\xi}$ in the proposed configuration are expected to be zero, but have nonzero values due to noise in the signal vector. For the comparison with the conventional systems, we assume a fixed level of constant electronic noise and changing magnitudes of signal-proportional shot noise, which simulates the effect of decreasing intensities in the lidar return with increasing probed distances.

Fig. 5 shows a comparison of the estimated uncertainties of the backscatter cross-sections Z_{11} and depolarization ratios as obtained from the four-channel configuration. The backscatter cross-sections Z_{11} determined in the two operation modes are virtually the same regardless of the noise level (the two curves lie on top of each other). For the case of low noise, assumed to consist of only electronic noise equal to 1% of Z_{11}, the four-channel system estimates Z_{11} with about 30% less uncertainty than the two-channel systems (the dashed line in the plot indicates equal uncertainties). This is due to the fact that with the

four-channel system a higher number of independent measurements is effectively used to determine Z_{11}. For situations with dominant shot noise, the uncertainty in Z_{11} is only marginally better in the four-channel system. (Note that the necessary additional beam splitters were accounted for when calculating the shot noise in the four-channel systems (50 : 50 beam splitters were assumed)).

The situation is different with respect to the uncertainties in the depolarization ratios: in the low-noise case, uncertainties are comparable and slightly larger in both four-channel configurations than in the two-channel configurations (8% and 17% for linear and circular depolarization ratios, respectively). With increasing shot-noise the performance of both operation modes degrades relative to the corresponding traditional system, however the relative uncertainties remain below a factor of two if the amount of shot noise remains less than ten times the amount of electronic noise. This degradation is associated with the correlations produced by the unequal measurement uncertainties (see eq. (**??**)) due to shot noise (the same effect would be produced by variations in electronic noise, but the example of shot noise is practically more relevant since electronic noise is typically small and well-controlled). Overall, the larger uncertainties in the depolarization ratios despite the larger number of simultaneous measurements stem from the somewhat lower sensitivity to the determination of the depolarization ratios, for a configuration that enables access to off-diagonal elements of the backscatter phase matrix.

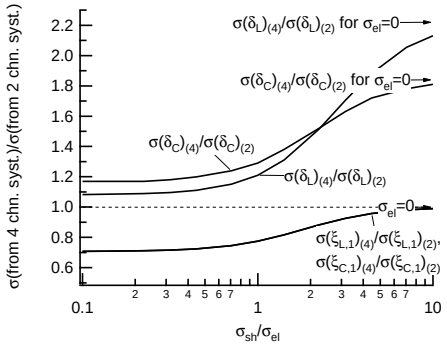

Figure 5: Comparison of the two-channel and four-channel systems: relative uncertainties in the estimated Z_{11} and linear and circular depolarization ratios from simulated cross-sections y_i, $i = 1, \ldots, 4$ with equivalent electronic noise $\sigma_{el,i} = 0.01\, Z_{11}$ and various levels of shot noise $\sigma^2_{sh,i} = k_i y_i$. Randomly oriented particles with an effective linear depolarization ratio $\delta_L = 0.175$.

Fig. 6 compares the four-channel and traditional systems in terms of uncertainties in the depolarization ratios for the entire range of linear depolarization ratios (for randomly oriented particulates). For this figure the non-zero elements of the backscatter phase matrix are calculated according to $Z_{22}/Z_{11} = (1-\delta_L)/(1+\delta_L)$, $Z_{33} = -Z_{22}$, and $Z_{44}/Z_{11} = 1 - 2Z_{22}/Z_{11}$ [22]. The uncertainties in measured depolarization ratios are similar for both four-channel operation modes for low and moderate levels of shot noise. In these situations, the depolarization ratios from measurements with the four-channel system have at most 20% higher uncertainties than those from the traditional system. At higher shot-noise levels, however, the four-channel measurements provide poor estimates of depolarization ratios for small and large underlying linear depolarization ratios. The four-channel system with circular incident light is less strongly affected by shot noise for true $\delta_L < 0.5$, but performs poorly for larger δ_L, with up to five times higher uncertainties in the estimated δ_C relative to measurements with the traditional system. In most practical cases, the linear depolarization ratio is less than 0.7; using circular polarized incident light appears thus better suited for shot noise-dominated measurements of aerosols containing only randomly oriented particles.

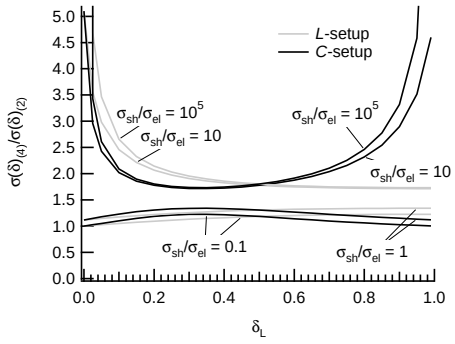

Figure 6: Comparison of the two-channel with the four-channel systems: relative uncertainties in linear and circular depolarization ratios from simulated cross-sections y_i as a function of the linear depolarization ratio $\delta_L = (Z_{11} - Z_{22})/(Z_{11} + Z_{22})$. Equivalent electronic noise $\sigma_{el,i} = 0.01\, Z_{11}$ with four levels of shot noise $\sigma_{sh,i}/\sigma_{el,i} = 0.1,\ 1,\ 10$, and 10^5.

4.2. Aerosols with preferential particle orientation

Fig. 7 depicts predictions of measured cross sections y_i from both four-channel configurations and for typical dust particles, assumed as 10 μm long prolate ellipsoids with aspect ratio 2 : 1. The orientation of 10% of the particles is assumed to be in exact alignment with a direction specified through the Euler angles α and β as described earlier. Compared with aerosols with completely randomly oriented particles, for which the measurable signals are by definition independent of orientation angles, the magnitudes of the measureable signals vary considerably with orientation. The perturbations in each channel amount to about 10% of the corresponding cross sections of completely randomly oriented particles (based on the calculated orientation-averaged (rms) deviations). In other words, if we knew that 10% of the particles are oriented in a particular, but unknown, direction, it would be appropriate to include additional systematic error on the order of 10% when interpreting the measured signals. (Note that it is a coincidence that the fraction of oriented particles and the level of systematic error are roughly the same; in general, particle shape, refractive index, size, and angular spread direction of preferred orientation determine the appropriate amount of systematic error.) The signals y_i show some of the structure of the backscatter matrix elements, which is to be expected for the assumed preferential orientation in directions without angular spread. The structures are less regular and asymmetric with respect to the orientation angles, however, as a consequence of y_i's being weighted sums of different backscatter phase matrix elements. From the ranges of the scale

bars, the expected signals in all channels are non-zero with similar relative ranges, but the orientation-averaged signals $y_{C,i}$ are somewhat more similar to each other than the $y_{L,i}$.

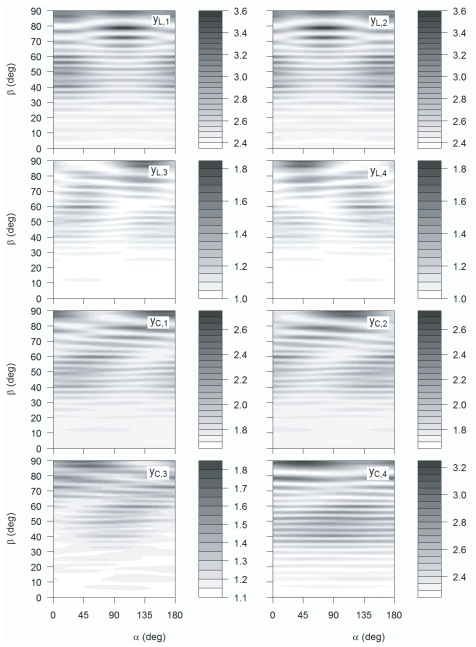

Figure 7: Calculated expected values of measured cross-sections y_i for 10% oriented particles as specified through azimuthal and polar angles α and β, respectively, mixed with 90% particles in random orientation. Particle properties are the same as for Fig. 2. Top four images: system with horizontal linear incident polarization; bottom four images: system with right circular incident polarization. For fully randomly oriented particulates the corresponding orientation-averaged cross sections are $\mathbf{y}_L = (2.65, 2.65, 1.12, 1.12)^t$, and $\mathbf{y}_C = (1.89, 1.89, 1.27, 2.51)^t$; orientation-averaged (rms) deviations are $\mathbf{s}_L = (0.24, 0.24, 0.12, 0.12)^t$ and $\mathbf{s}_C = (0.18, 0.18, 0.12, 0.21)^t$.

Fig. 8 shows the ratios derived from the expected cross sections depicted in Fig. 7. Preferential orientation clearly affects the magnitude of depolarization ratios. Again from calculated orientation-averaged rms deviations, 14% and 10% variability relative to the ratios for completely randomly oriented particles, respectively, for the systems with linear and circular polarized incident light is indicated. Given the symmetry properties of the particles, the circular depolarization ratios become independent of the azimuthal angle α. The relative ratios $d_{L,3} = \xi_{L,3}/2\xi_{L,1}$, $d_{L,4} = \xi_{L,4}/2\xi_{L,1}$, and $d_{C,2} = \xi_{C,2}/2\xi_{C,1}$, $d_{C,3} = \xi_{C,3}/2\xi_{C,1}$ yield values in the ranges ± 0.09 and ± 0.11, respectively, indicating that both systems are capable of flagging presence of preferentially oriented particles. Existence of "blind spots", that is, false reporting of absence of preferential orientation, is, however, an consequence of the ranges spanning from negative to positive values.

Since the off-diagonal ratios $d_{L,2}$, $d_{L,3}$, $d_{C,2}$, and $d_{C,3}$ are zero when all particles are oriented randomly, proper interpretation of the reported ratios requires proper estimation of the uncertainties as outlined earlier. The ability of flagging the presence of preferentially oriented particles is illustrated in Fig. 9, which shows by what factor the combined parameters $R_L = (\xi_{L,3}^2 + \xi_{L,4}^2)^{1/2}$ and $R_C = (\xi_{C,2}^2 + \xi_{C,3}^2)^{1/2}$ are larger than the standard deviation of noise for two levels of measurement

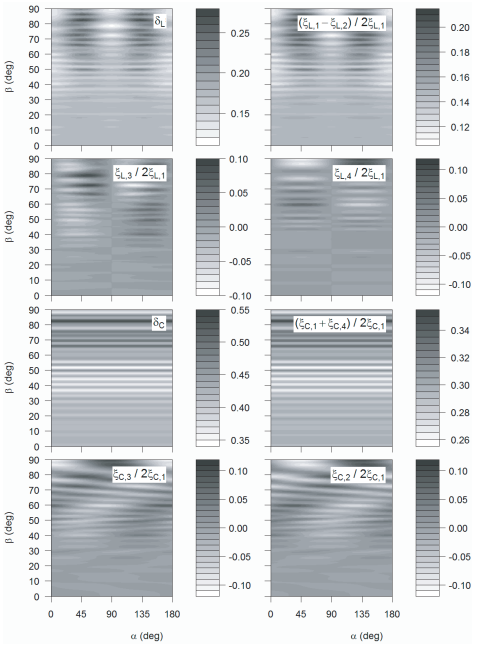

Figure 8: Retrieved parameter ratios for 10% oriented particles mixed with 90% particles in random orientation, corresponding to the expected signals shown in Fig. 7. Top four images: system with horizontal linear incident polarization; bottom four images: system with right circular incident polarization. The orientation-averaged ratios are $(\delta_L, d_{L,1}, d_{L,2}, d_{L,3}) = (0.176, 0.150, 0, 0)$, and $(\delta_C, d_{C,1}, d_{C,2}, d_{C,3}) = (0.427, 0.299, 0, 0)$; the respective orientation-averaged (rms) deviations are $(0.024, 0.017, 0.024, 0.026)$ and $(0.041, 0.020, 0.032, 0.032)$.

noise. The ranges for the combined ratios are essentially the same for the two systems, with up to 15.2 and 2.4 for the low and high noise situations, respectively. As shown in Fig. 9, preferential orientation of prolate spheroids is increasingly difficult to detect for smaller polar angles β (*i.e.* the axis of rotation is nearly aligned with the direction of light propagation). For the *L*-setup all backscatter matrix elements that enter the calculation of R_L vanish for particular azimuthal angles. This is not the case for the *C*-setup, adding another reason to prefer the *C*-setup for a four-channel system. The excellent performance at the low levels of noise suggests that both operation modes can provide information about particulate orientation, but the ability to detect preferential orientation can be severely impaired when only noisy measurements are available.

4.3. Aerosol with small numbers of randomly oriented particles

Another example of the utility of information from the four-channel system is the case of insufficiently large numbers of particles. While in this case the particles are essentially randomly oriented, off-diagonal backscatter phase matrix elements are not completely nullified during the superposition of all individual phase matrices. For typical atmospheric lidar systems, which probe volumes on the order of 1m^3 in size, this situation might occur only with mm-sized objects because the contribution from the gas background (and fine dust particles) dominates the lidar signals otherwise. However, when applying short range lidar systems with ultra-short pulses (several

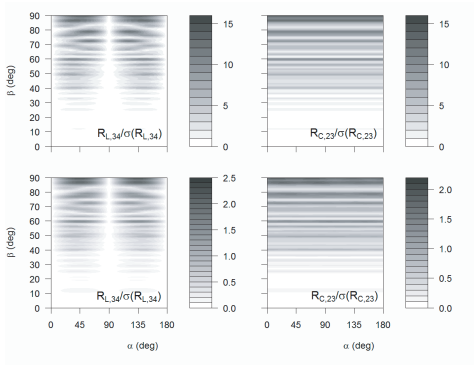

Figure 9: Signal-to-noise ratios for the combined off-diagonal parameters for 10% oriented particles mixed with 90% particles in random orientation, corresponding to the expected signals shown in Fig. 7. Top panels: σ_{el} equal to 1% of the orientation-averaged backscatter coefficient Z_{11}, negligible shot noise $\sigma_{sh} = 0.1\sigma_{el}$; bottom panels: shot noise-dominated measurements, σ_{el} equal to 1% of the orientation-averaged backscatter coefficient Z_{11}, $\sigma_{sh} = 10\sigma_{el}$.

picoseconds) [41, 42] cm^3-sized volumes are sampled (corresponding to of a few millimeters spatial range resolution); one might therefore encounter the small-statistical-sample problem more frequently even with dust-like particulates. To illustrate this aspect, we show simulation results for the limiting case of dominant signal contributions by particles in Fig. 10 (the backscattering from gas molecules is assumed to be negligible).

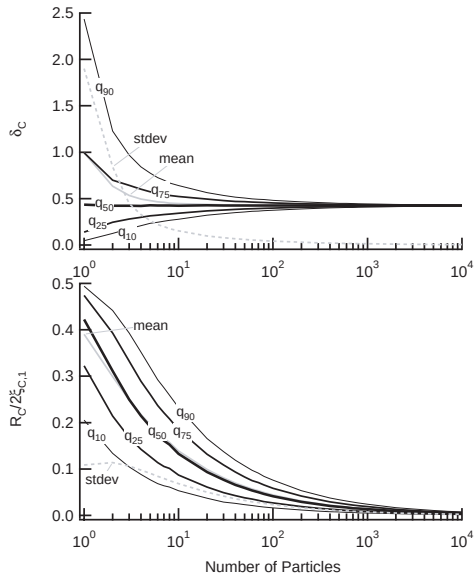

Figure 10: Effect of the number of particles in the probed volume on depolarization ratio and combined off-diagonal parameter for the system with circular polarized incident light. Particle properties are the same as for Fig. 2. Top image: depolarization ratio δ_C; bottom image: $r_C = (\xi_{C,2}^2 + \xi_{C,3}^2)^{1/2}/2\xi_{C,1}$. The orientation angles of the corresponding number of particles were chosen at random by sampling from a uniform distribution of orientation directions ($\alpha \sim \mathrm{Unif}(0, 2\pi)$, $(1 - \cos\beta)/2 \sim \mathrm{Unif}(0, 1)$) for each of 10000 repetitions.

As shown in the top panel of Fig. 10, the depolarization ratios converge to a constant value with increasing number of particles in the probed volume. With less than 100 particles in the probed volume, the range of observed depolarization ratios widens considerable as the number of particles decreases (for instance, the difference between the 10 and 90% quantiles indicates that for ten or fewer particles, less than 80% of the observations lie between 0.27 and 0.64, or about ±40% from the expected value for large populations). The increase of the mean value towards smaller sizes indicates that the depolarization ratio is on average over-estimated if fewer than ten particles are sampled. The standard deviations from the 10000 samples per particle number further show that appropriate uncertainties of measured depolarization ratios are larger than 35% if fewer than 100 particles are present in the lidar probed sample. In addition to the depolarization ratio, the four-channel system enables evaluation of the magnitudes of off-diagonal elements, as shown in the bottom panel of Fig. 10. The relative magnitudes $R_C/2\xi_{C,1} = (\xi_{C,2}^2 + \xi_{C,3}^2)^{1/2}/2\xi_{C,1}$ decrease to zero with increasing particle numbers, but in contrast to the depolarization ratio the decay is more gradual and the curves of constant quantiles are monotonically decreasing functions of the particle number. This behavior is useful for characterizing the number concentration of particles, in particular when complementary information concerning the optical properties of the particulates is available. For the simulated aerosol, an observed $R_C/2\xi_{C,1} = 0.1$ translates to $3 - 50$ particles as an 80% confidence interval for the particle number, for example.

5. Conclusions

In this theoretical study we investigated a four-channel polarization lidar system with particular focus on detection of preferentially oriented aerosol particles. The presented system concept facilitates temporally and spatially resolved measurements of combinations of backscattering phase matrix elements for quantification of aerosol particle orientation in addition to measurements of backscatter cross-sections and depolarization ratios. The proposed system is free of moving parts, which simplifies calibration as well as data processing and eliminates systematic errors associated with asynchronous polarimetric measurements. The system, which yields minimum condition numbers of the design matrix, performs better with respect to backscatter cross-sections than traditional two-channel systems. While somewhat higher levels of uncertainty have to be accepted for the measured depolarization ratios, the four-channel system is capable of providing information on preferential orientation and the presence of small numbers of nonspherical particles. In particular, operation with circular polarized incident light appears advantageous as noise transmission characteristics and reliability with respect to detection of preferential particle orientation are better than with linear polarized light. Uncertainties analysis revealed that both signal-independent noise and photon shot noise in the measurements propagate through the signal inversion process to the estimated parameters with little amplification. As a consequence, limitations for detection of preferential orientation are directly related to the amount of measurement noise, and thus can be minimized by application of high-quality system hardware and advanced signal-denoising techniques. Finally, the discussed four-channel system can offer complementary information about particle number counts in the probed volume ele-

ment, particularly in lidar applications with an ultra-short pulse laser beam.

Acknowledgements

Support by Sandia National Laboratories' LDRD (Laboratory Directed Research and Development) is gratefully acknowledged. Sandia National Laboratories is a multi-program laboratory managed and operated by Sandia Corporation, a wholly owned subsidiary of Lockheed Martin Corporation, for the U.S. Department of Energy's National Nuclear Security Administration under contract DE-AC04-94AL85000.

References

[1] U. Wandinger, Introduction to lidar, in: C. Weitkamp (Ed.), Lidar, Springer-Verlag, New York, 2005, pp. 1–18.
[2] K. Sassen, Polarization in lidar, in: C. Weitkamp (Ed.), Lidar, Springer-Verlag, New York, 2005, pp. 19–42.
[3] M. Del Guasta, E. Vallar, O. Riviere, F. Castagnoli, V. Venturi, M. Morandi, Use of polarimetric lidar for the study of oriented ice plates in clouds, Applied Optics 45 (2006) 4878–4887.
[4] K. Sassen, Lidar backscatter depolarization technique for cloud and aerosol research, in: M. I. Mishchenko, J. W. Hovenier, L. D. Travis (Eds.), Light Scattering by Nonspherical Particles: Theory, Measurements, and Geophysical Applications, Academic Press, San Diego, 2000, pp. 393–415.
[5] K. Sassen, The polarization lidar technique for cloud research: A review and current assessment, Bulletin of the American Meteorological Society 72 (1991) 1848–1866.
[6] L. R. Poole, G. S. Kent, M. P. McCormic, W. H. Hunt, M. T. Osborn, S. Schaffner, M. C. Pitts, Dual-polarization airborne lidar for observation of polar stratospheric cloud evolution, Geophysical Research Letters 17 (1990) 389–392.
[7] K. Sassen, Polarization diversity lidar returns from virga and precipitation: Anomalies and the bright band analogy, Journal of Applied Meteorology 15 (1976) 292–300.
[8] R. M. Schotland, K. Sassen, R. Stone, Observations by lidar of linear depolarization ratios for hydrometeors, Journal of Applied Meteorology 10 (1971) 1011–1017.
[9] M. I. Mishchenko, J. W. Hovenier, Depolarization of light backscattered by randomly oriented nonspherical particles, Optics Letters 20 (1995) 1356–1358.
[10] G. David, B. Thomas, T. Nousiainen, A. Miffre, P. Rairoux, Retrieving simulated volcanic, desert dust and sea-salt particle properties from two/three-component particle mixtures using uv-vis polarization lidar and t matrix, Atmospheric Chemistry and Physics 13 (2013) 6757–6776.
[11] B. V. Kaul, I. V. Samokhvalov, S. N. Volkov, Investigating particle orientation in cirrus clouds by measuring backscattering phase matrices with lidar, Applied Optics 43 (2004) 6620–6628.
[12] N. Mahowald, D. S. Ward, S. Kloster, M. G. Flanner, C. L. Heald, N. G. Heavens, P. G. Hess, J.-F. Lamarque, P. Y. chuang, Aerosol impacts on climate and biogeochemistry, Annual Review of Environment and Resources 36 (2011) 45–74.
[13] A. H. Auer, D. L. Veal, The dimension of ice crystals in natural clouds, Journal of the Atmospheric Sciences 27 (1970) 919–926.
[14] J. D. Klett, Orientation model for particles in turbulence, Journal of the Atmospheric Sciences 52 (1995) 2276–2285.
[15] Z. Ulanowski, J. Bailey, P. W. Lucas, J. H. Hough, E. Hirst, Alignment of atmospheric mineral dust due to electric field, Atmospheric Chemistry and Physics 7 (2007) 6161–6173.
[16] R. A. Chipman, Polarimetry, in: M. Bass (Ed.), Handbook of Optics, 2nd Edition, McGraw-Hill, 1995.
[17] S. R. Pal, A. I. Carswell, Polarization properties of lidar backscattering from clouds, Applied Optics 12 (1973) 1530–1535.
[18] J. D. Houston, A. I. Carswell, Four-component polarization measurement of lidar atmospheric scattering, Applied Optics 17 (1978) 614–620.
[19] C. J. Flynn, A. Mendoza, Y. Zheng, S. Mathur, Novel polarization-sensitive micropulse lidar measurement technique, Optics Express 15 (2007) 2785–2790.
[20] M. Hayman, S. Spuler, B. Morley, J. VanAndel, Polarization lidar operation for measuring backscatter phase matrices of oriented scatters, Optics Express 20 (2012) 29553–29567.
[21] K. M. Twietmeyer, R. A. Chipman, Optimization of mueller matrix polarimeters in the presence of error sources, Optics Express 16 (2008) 11589–11603.
[22] M. I. Mishchenko, J. W. Hovenier, L. D. Travis (Eds.), Light Scattering by Nonspherical Particles, Academic Press, San Diego, 2000.
[23] M. I. Mishchenko, Calculation of the amplitude matrix for a nonspherical particle in a fixed orientation, Applied Optics 39 (2000) 1026–1031.
[24] C.-R. Hu, G. W. Kattawar, M. E. Parkin, P. Herb, Symmetry theorems on the forward and backward scattering mueller matrices for light scattering from a nonspherical dielectric scatterer, Applied Optics 26 (1987) 4159–4173.
[25] M. I. Mishchenko, L. D. Travis, T-matrix computations of light scattering by large spheroid particles. theory, measurements, and applications, Optics Communications 109 (1994) 16–21.
[26] M. I. Mishchenko, L. D. Travis, A. Macke, Scattering of light by polydisperse, randomly oriented, finite circular cylinders, Applied Optics 35 (1996) 4927–4940.
[27] D. J. Wielaard, M. I. Mishchenko, A. Macke, B. E. Carlson, Imporved t-matrix computations for large, nonabsorbing and weakly absorbing nonspherical particles and comparison with geometrical optics approximation, Applied Optics 36 (1997) 4305–4313.
[28] M. I. Mishchenko, Extended-precision t-matrix code for nonspherical particles in a fixed orientation, `http://www.giss.nasa.gov/staff/mmishchenko/t_matrix.html`, accessed in April 2013 (2005).
[29] T. c. Bond, R. W. Berstrom, Light absorption by carbonaceous particles: An investigative review, Aerosol Science and Technology 40 (2006) 27–67.
[30] C. F. Bohren, D. R. Huffman, Absorption and Scattering of Light by Small Particles, John Wiley & Sons, Inc., 1983.
[31] G. G. Gimmestad, Reexamination of depolarization in lidar measurements, Applied Optics 47 (2008) 3795–3802.
[32] K. Lange, Numerical Analysis for Statisticians, 2nd Edition, Springer, New York, 2010.
[33] L. N. Trefethen, D. Bau III, Numerical Linear Algebra, Society for Industrial and Applied Mathematics, Philadelphia, 1997.
[34] L. Scrucca, GA: A package for genetic algorithms in R, Journal of Statistical Software 53 (4) (2013) 1–37.
URL `http://www.jstatsoft.org/v53/i04/`
[35] R. H. Byrd, P. Lu, J. Nocedal, C. Zhu, A limited memory algorithm for bound constrained optimization, SIAM Journal of Scientific Computing 16 (1995) 1190–1208.
[36] R Core Team, R: A language and environment for statistical computing, `http://www.R-project.org/` (2013).
[37] R. M. A. Azzam, I. M. Elminyawi, A. M. El-Saba, General analysis and optimization of the four-detector photopolarimeter, Journal of the Optical Society of America A 5 (1988) 681–689.
[38] Hamamatsu, Photomultiplier Tubes - Basics and Applications, 2nd Edition, Hamamatsu Photonics K. K., Hamamatsu City, Japan, 1999.
[39] R. Christensen, Advanced Linear Modeling. Multivariate, Time Series, and Spatial Data; Nonparametric Regression and Response Surface Maximization, 2nd Edition, Springer Verlag, New York, 2001.
[40] G. Casella, R. L. Berger, Statistical Inference, 2nd Edition, Thomson Learning, Stamford, CT, 2001.
[41] B. Kaldvee, A. Ehn, J. Bood, M. Aldén, Development of a picosecond lidar system for large-scale combustion diagnostics, Applied Optics 48 (2009) B65–B72.
[42] B. Kaldvee, J. Bood, M. Aldén, Picosecond-lidar thermometry in a measurement volume surrounded by highly scattering media, Measurement Science and Technology 22 (2011) 125302(9pp).